

PAPER

## Facile fabrication of 3D porous MnO@GS/CNT architecture as advanced anode materials for high-performance lithium-ion battery

To cite this article: Junyong Wang *et al* 2018 *Nanotechnology* **29** 315403

View the [article online](#) for updates and enhancements.

### Related content

- [Free-anchored Nb<sub>2</sub>O<sub>5</sub>@graphene networks for ultrafast-stable lithium storage](#)  
Qinglin Deng, Mengjiao Li, Junyong Wang et al.
- [Three-dimensional nitrogen and sulfur co-doped holey-reduced graphene oxide frameworks anchored with MoO<sub>2</sub> nanodots for advanced rechargeable lithium-ion batteries](#)  
Jie Pei, Hongbo Geng, Huixiang Ang et al.
- [In situ preparation of Fe<sub>3</sub>O<sub>4</sub> in a carbon hybrid of graphene nanoscrolls and carbon nanotubes as high performance anode material for lithium-ion batteries](#)  
Yuwen Liu, Ahmad Hassan Siddique, Heran Huang et al.

# Facile fabrication of 3D porous MnO@GS/CNT architecture as advanced anode materials for high-performance lithium-ion battery

Junyong Wang<sup>1</sup>, Qinglin Deng<sup>1</sup>, Mengjiao Li<sup>1</sup>, Cong Wu<sup>1</sup>, Kai Jiang<sup>1,3</sup>,  
Zhigao Hu<sup>1,2,3</sup> and Junhao Chu<sup>1</sup>

<sup>1</sup> Key Laboratory of Polar Materials and Devices (MOE) and Technical Center for Multifunctional Magneto-Optical Spectroscopy (Shanghai), Department of Electronic Engineering, East China Normal University, Shanghai 200241, People's Republic of China

<sup>2</sup> Collaborative Innovation Center of Extreme Optics, Shanxi University, Taiyuan, Shanxi 030006, People's Republic of China

E-mail: [kjiang@ee.ecnu.edu.cn](mailto:kjiang@ee.ecnu.edu.cn) and [zghu@ee.ecnu.edu.cn](mailto:zghu@ee.ecnu.edu.cn)

Received 11 March 2018, revised 10 May 2018

Accepted for publication 14 May 2018

Published 1 June 2018



## Abstract

To overcome inferior rate capability and cycle stability of MnO-based anode materials for lithium-ion batteries (LIBs), we reported a novel 3D porous MnO@GS/CNT composite, consisting of MnO nanoparticles homogeneously distributed on the conductive interconnected framework based on 2D graphene sheets (GS) and 1D carbon nanotubes (CNTs). The distinctive architecture offers highly interpenetrated network along with efficient porous channels for fast electron transfer and ionic diffusion as well as abundant stress buffer space to accommodate the volume expansion of the MnO nanoparticles. The MnO@GS/CNT anode exhibits an ultrahigh capacity of  $1115 \text{ mAh g}^{-1}$  at  $0.2 \text{ A g}^{-1}$  after 150 cycles and outstanding rate capacity of  $306 \text{ mAh g}^{-1}$  at  $10.0 \text{ A g}^{-1}$ . Moreover, a stable capacity of  $405 \text{ mAh g}^{-1}$  after 3200 cycles can still be achieved, even at a large current density of  $5.0 \text{ A g}^{-1}$ . When coupled with  $\text{LiMn}_2\text{O}_4$  (LMO) cathode, the LMO || MnO@GS/CNT full cell characterizes an excellent cycling stability and rate capability, indicating the promising application of MnO@GS/CNT anode in the next-generation LIBs.

Supplementary material for this article is available [online](#)

Keywords: MnO, graphene sheets, CNT, ultrahigh capacity, cycling stability

(Some figures may appear in colour only in the online journal)

## 1. Introduction

Rechargeable lithium-ion batteries (LIBs) are currently considered as efficient energy storage technologies for integration of large-scale renewable energy and for portable electronics due to their high energy density, safety, and low environmental impacts [1–4]. Although graphite anodes used in LIBs have gained commercial success, the limited theoretical

capacity ( $372 \text{ mAh g}^{-1}$ ) is far from fulfilling the key demands of energy-intensive equipment and electric vehicles [5]. Therefore, it is highly essential to develop alternative anode materials with high reversible capacity, good rate capability, and desired cycle stability for promoting the development of the next-generation LIBs. In this regard, transition metal oxides (TMOs) with a conversion reaction mechanism have been demonstrated as attractive candidate anode materials in terms of their high theoretical capacity, excellent electrical behavior, and resource abundance [6–16]. Among the various

<sup>3</sup> Authors to whom any correspondence should be addressed.

TMOs anodes for LIBs, manganese monoxide ( $\text{MnO}$ ), have attracted extensive attention due to its high theoretical capacity ( $756 \text{ mAh g}^{-1}$ ), high energy density ( $5.43 \text{ g cm}^{-3}$ ), low operation potential (1.032 V, versus Li/Li $^{+}$ ), voltage hysteresis (<0.7 V), and nontoxicity [17–21]. However, the key challenges associated with the practical application of  $\text{MnO}$  anode are its inferior rate capability and rapid capacity fading, which is mainly attributed to its low intrinsic electric conductivity and large volume expansion/contraction during the repeated conversion processes [17, 22, 23]. In particular, since  $\text{MnO}$  could react with lithium to form  $\text{Mn}/\text{Li}_2\text{O}$  matrix, the drastic pulverization of  $\text{MnO}$  anodes is aggravated by severe agglomeration and volume changes, leading to lower reversible capacities and poorer cycle life [19, 24].

To date, tremendous efforts have been focused on the synthesis of nano-architectures electrode materials and the design of various morphologies, like nanowires [25, 26], nanospheres [27, 28], nanotubes [19], nanorods [29, 30], and nanopeapod [31], for enhancing the electrochemical properties of  $\text{MnO}$ -based materials as LIB anodes. The sagacious design of nanostructures could effectively relieve the structural strain induced by the conversion process and accelerate the transport of ion/electron for providing additional channels along with reducing the diffusion distance, resulting in high-rate performance. However, the cycling performance is still limited owing to the self-aggregation of  $\text{MnO}$  nanoparticles and the undesirable electrode/electrolyte reactions. In order to address the above problems, hybridizing and coating metal oxides with functional carbon matrix have been demonstrated to enhance the cycling stability of  $\text{MnO}$ -based anodes [32–36]. Because those strategy can meritiously aggrandize the surface area, ameliorate the electrical conductivity, significantly alleviate the aggregation of  $\text{MnO}$  and the volume variation upon the cycle processes. Although many progresses have been achieved, the cycle life of such anode materials for LIBs is still unsatisfactory for practical applications.

Recently, the robust three-dimensional (3D) hierarchical composites have been reported to further improve or/and optimize the electrochemical performance by encapsulating and anchoring the  $\text{MnO}$  nanoparticles into 3D conductive frameworks. For example, 3D porous  $\text{MnO@CF}$  with excellent structure stability presented relatively high specific capacity of  $939 \text{ mAh g}^{-1}$  at  $0.2 \text{ A g}^{-1}$  over 200 cycles and excellent rate capability of  $560.2 \text{ mAh g}^{-1}$  at  $4.0 \text{ A g}^{-1}$  [37]. 3D porous  $\text{MnO/C-N}$  nanoarchitecture exhibited high specific capacity ( $756.5 \text{ mAh g}^{-1}$  at  $0.1 \text{ A g}^{-1}$ ) and long-life span ( $513.0 \text{ mAh g}^{-1}$  after 400 cycles at  $0.3 \text{ A g}^{-1}$ ) [38]. 3D porous  $\text{MnO@N-GSC/GR}$  configuration composed of ultralong 1D  $\text{MnO}$  nanowires sheathed in N-doped GSCs with 2D N-doped graphene ribbons showed ultrahigh rate capability ( $205 \text{ mAh g}^{-1}$  at  $15.0 \text{ A g}^{-1}$ ) and long-life span ( $812 \text{ mAh g}^{-1}$  after 1000 cycles at  $2.0 \text{ A g}^{-1}$ ) [39]. As expected, 3D porous carbon frameworks determine high specific surface area, effective buffer space, and availability/penetrability of electrolyte, which can greatly improve the charge transfer kinetics and the electrochemical activity of  $\text{MnO}$  nanoparticles. Therefore, one promising strategy to

obtain superior electrochemical performance is to engineer a robust 3D cross-linked architecture by a simple and efficient method, which is imperative for the practical application of highly stable  $\text{MnO}$ -based anodes in LIBs.

Herein, in pursuing outstanding cycling stability and rate capability, we have rationally designed a 3D nanohybrid architecture as anode materials for high-performance LIBs, which is based on  $\text{MnO}$  nanoparticles assembled with the cross-linked networks constructed by 1D carbon nanotubes (CNT) and 2D graphene sheets (GS). This electrode is prepared via a one-step hydrothermal process and subsequent thermal treatment, yielding the ternary nanocomposite  $\text{MnO@GS/CNT}$ . As expected, the  $\text{MnO}$  nanoparticles are homogenously embedded in the electroactive materials, which could facilitate the conversion reaction kinetics over the shorter diffusion lengths of lithium ions and remittent volume change of  $\text{MnO}$  during cycling. At the same time, the  $\text{MnO}$  nanoparticles ensure stable formation of solid electrolyte interface (SEI), which avoids atom migration and enhances the structural integrity during cycling, leading to partially confined electrochemical reactions and hence long-term cycling stability. Moreover, the 3D conductive architecture can endow smooth ion transportation, higher electrochemical responses, and lesser volume change by merits of their strong mechanical integrity, multidirectional channels, and buffer space. As a result, such 3D  $\text{MnO@GS/CNT}$  electrode shows high specific capacity and excellent rate capability. Strikingly, a reversible capacity of  $405 \text{ mAh g}^{-1}$  after 3200 cycles is remained at high current density of  $5.0 \text{ A g}^{-1}$ , showing superior long-term cycling stability. For practical evaluation of the  $\text{MnO@GS/CNT}$  anode material, all-manganese-based LIB full cell was assembled by coupling  $\text{LiMn}_2\text{O}_4$  (LMO) nanoparticles as the cathode. The LMO ||  $\text{MnO@GS/CNT}$  full cell exhibits excellent rate performance and cycling stability, demonstrating a highly attractive candidate for applications in advanced LIBs.

## 2. Experimental section

### 2.1. Material preparation

GSs were prepared from natural graphite powder by the modified Hummer's approach. CNT were obtained from XFNANO Materials Tech Co., Ltd (Nanjing, China) and treated in a mixture of concentrated  $\text{H}_2\text{SO}_4/\text{HNO}_3$  (3:1) at  $80^\circ\text{C}$  under constant magnetic stirring for 2 h. The as-prepared CNT were purified by centrifuging and washing with deionized (DI) water to remove the residual acid, and then the acidified CNT were obtained upon vacuum drying at  $60^\circ\text{C}$ . The 3D  $\text{MnO@GS/CNT}$  composite was prepared using a simple one-step hydrothermal method. In a typical procedure, 20 mg CNT were first added to 60 ml GS aqueous dispersion ( $1 \text{ mg mL}^{-1}$ ). The mixture was intensively ultra-sonicated using an ultrasonication probe (1000 W) for 30 min to form a uniform GS/CNT suspension. Then 0.2 g ascorbic acid, 1 mmol  $\text{Mn}(\text{Ac})_2 \cdot 4\text{H}_2\text{O}$  and 4 g NaOH were added into the GS/CNT suspension orderly, following stirred for 2 h. After

that, the homogeneous mixed solution was sealed in a 100 ml autoclave at 180 °C for 12 h. After the autoclave cooling to room temperature, the products were collected and washed by DI water and absolute alcohol alternately. Finally, the MnO@GS/CNT samples were obtained by vacuum dried at 60 °C for 12 h and calcined in a tube furnace at 600 °C for 2 h under a N<sub>2</sub> atmosphere. For comparison, pure MnO and GS/CNT composites were synthesized at the same condition without corresponding additive. For preparing LiMn<sub>2</sub>O<sub>4</sub> nanoparticles, Mn(Ac)<sub>2</sub> · 4H<sub>2</sub>O and Li(Ac)<sub>2</sub> · 2H<sub>2</sub>O with a molar ratio of 2:1.1 were dissolved in absolute alcohol and magnetic stirred for 2 h. The solution was then evaporated under 100 °C to obtain a dried powder mixture, following calcined in a tube furnace at 750 °C in air for 2 h.

## 2.2. Materials characterization

Scanning electron microscopy (SEM) measurements were performed on PHILIPS XL30TMP. Transmission electron microscopy (TEM) studies were conducted on a FEI Tecnai G2 20TWIN electron microscope at the operating voltage of 200 kV. X-ray diffraction (XRD) analysis were measured on a Bruker D8 diffractometer equipped with Cu-Kα radiation ( $\lambda = 1.5418 \text{ \AA}$ ) at a generator voltage of 40 kV and a generator current of 20 mA with a scanning speed of 10° min<sup>-1</sup> from 10° to 80°. Raman scattering measurement was carried out using a micro-Raman spectrometer (Jobin-Yvon LabRAM HR 800UV) with excitation laser beam wavelength of 632.8 nm. Thermogravimetric analysis (TGA) was tested at TA instruments with a ramp rate of 10 °C min<sup>-1</sup> under 50 ml min<sup>-1</sup> of flowing air. X-ray photoelectron spectroscopy (XPS) was conducted on a RBD upgraded PHI-5000C ESCA system (Perkin-Elmer) with Mg-Kα radiation ( $h\nu = 1253.6 \text{ eV}$ ), and binding energies were calibrated by using the containment carbon (C 1s = 284.6 eV). The nitrogen adsorption/desorption isotherms, Brunauer–Emmett–Teller (BET) surface area and DFT pore size distribution were measured by TriStar II 3020 instrument.

## 2.3. Electrochemical measurement

The electrochemical performance of the MnO@GS/CNT and LiMn<sub>2</sub>O<sub>4</sub> composites were recorded in 2025 coin-type cells. LiPF<sub>6</sub> (1 M) dissolved in ethylene carbonate/dimethyl carbonate/ethyl methyl carbonate (1:1:1, in vol) was used as the electrolyte and Cellgard 2400 was used as the separator. The anode and cathode were prepared by pasting homogeneous slurries consisting of the as-prepared materials (80 wt%), acetylene black (10 wt%), and polyvinylidene fluoride binder (10 wt%) dissolved in N-methyl-2-pyrrolidone onto pure Cu and Al foils, respectively, followed by vacuum dried at 100 °C for 12 h. The mass loading of the active material in the MnO@GS/CNT anode for half-cell was about 1.0 mg cm<sup>-2</sup>. And the mass loading of the active material in the testing full cell were controlled at around 0.7 mg cm<sup>-2</sup> for MnO@GS/CNT anode and 2.1 mg cm<sup>-2</sup> for the LiMn<sub>2</sub>O<sub>4</sub> cathode, respectively. Coin half cells were assembled by using the lithium foil as the counter electrode in an argon-filled

glovebox with the concentrations of moisture and oxygen below 1 ppm. Prior to full cell assembly, the MnO@GS/CNT anode was prelithiated by placing the electrode in direct contact with a Li foil in the electrolyte solution for 4 h. Then the lithiated anode was assembled with LiMn<sub>2</sub>O<sub>4</sub> cathode to constitute a full cell using the same assembling process as in the half-cell assembly. The galvanostatic charge–discharge tests were conducted on Land CT 2001A battery testing system at various current densities. Cyclic voltammetry (CV) tests were recorded on a CHI660D electrochemical workstation at various scan rates and electrochemical impedance spectroscopy (EIS) was obtained using CHI 760D electrochemical workstation by applying a sine wave with amplitude of 5 mV over the frequency range from 100 kHz to 0.01 Hz.

## 3. Results and discussion

### 3.1. Surface morphologies

Figure 1(a) shows a typical SEM image of the cross-linked morphology of the MnO@GS/CNT nanocomposite. The size of the 3D nanohybrid architectures was in the range of 4–10 μm, similar to that of GS/CNT composite (see the SI, figure S1 available online at [stacks.iop.org/NANO/29/315403/mmedia](https://stacks.iop.org/NANO/29/315403/mmedia)). There is no apparent difference in the surface morphology between MnO@GS/CNT and GS/CNT, elucidating that MnO might be embedded into the GS/CNT matrix. In addition, the surfaces of MnO@GS/CNT structure are very rough with many microscopic voids, which might bring more active sites for electrode surface reactions and buffer space for volume change. With randomly distributed CNT, this architecture would be beneficial to link the electrode materials and electrolytes, thus boosting the rapid transfer of ion and electron. The uniformly distributed nanoparticles on the conductive networks effectively suppress the agglomeration of MnO and increase the utilization of the active metal oxides. The high-magnification SEM images in figure 1(b) and S2, marked by a dotted red square in figure 1(a), further reveal that the MnO@GS/CNT nanocomposite are actually the aggregation of MnO nanoparticles, CNT, and GSs. The nanoscale structure will be greatly conducive to release more pseudocapacitance of MnO due to the felicitously distributed MnO nanoparticles. The detailed structures of MnO@GS/CNT nanocomposite were further characterized by TEM. Figure 1(c) is a typical TEM image of MnO@GS/CNT, clearly showing that MnO grains (dark zones) are anchored to the carbon matrix (bright zones). The existence of nanocrystalline MnO and carbon matrix is confirmed by their corresponding selected area electron diffraction (SAED) patterns (see figure 1(f), marked with a dotted blue circle in figure 1(c)). The corresponding ring-like SAED patterns can be indexed as the (111), (200), (220), and (222) planes of cubic MnO and GSs. The high-resolution TEM (HRTEM) images (figures 1(d) and (e)) further reveal the clear lattice fringes with d-spacing of 0.224 and 0.258 nm, corresponding to the (111) and (200) planes of cubic-phase MnO. Moreover, conductive carbon matrix are clearly

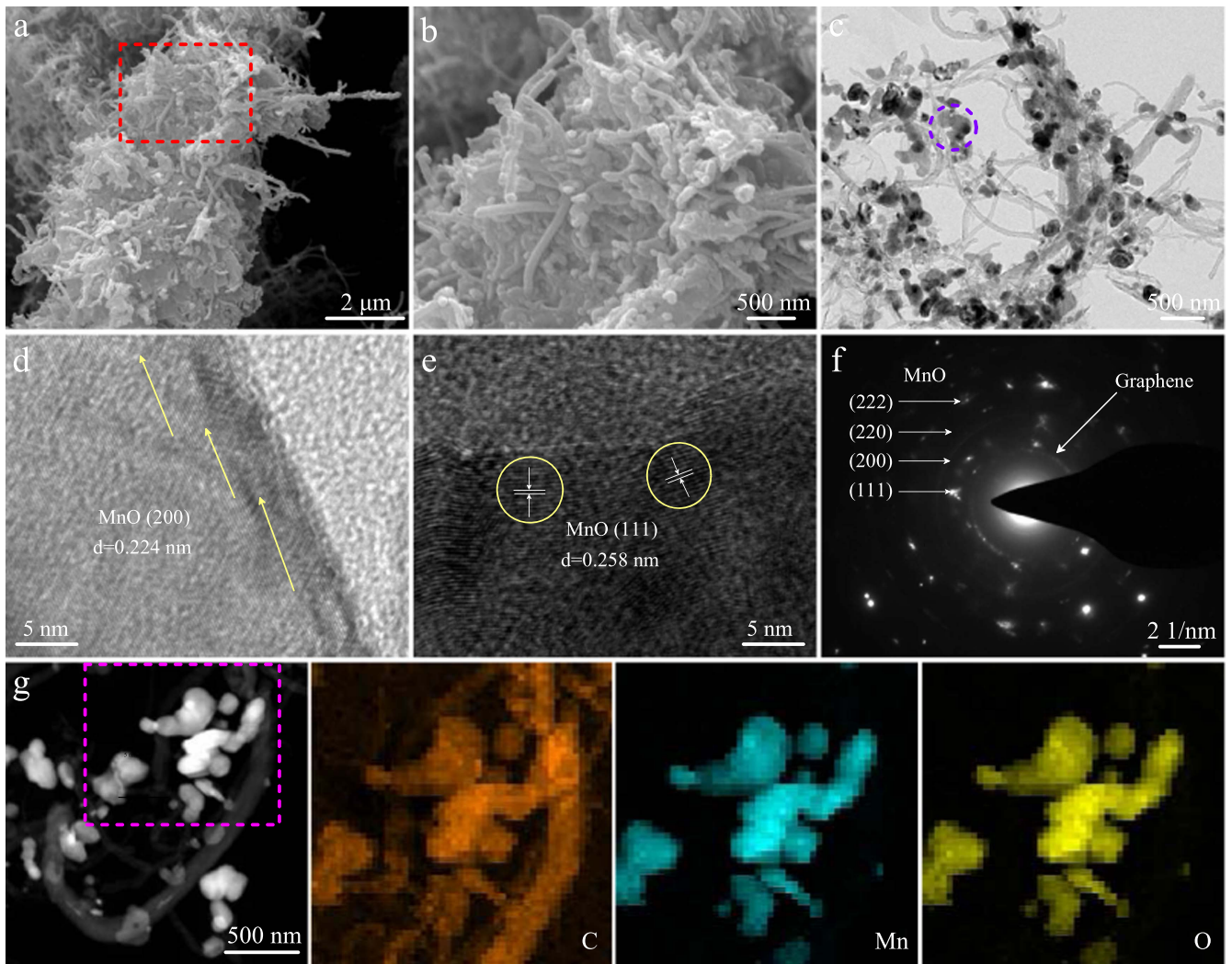


**Figure 1.** (a) Typical SEM image of MnO@GS/CNT composite; (b) high-magnification SEM image showing a small zone of MnO@GS/CNT composite; (c) typical TEM image of MnO@GS/CNT composite; (d)–(e) high-resolution TEM image of MnO@GS/CNT composite; (f) selected area electron diffraction (SAED) patterns; (g) TEM image and corresponding EDS mappings of MnO@GS/CNT composite.

visualized in the HRTEM image, which would be beneficial for electrochemical performances. Specifically, the TEM image of MnO@GS/CNT along with corresponding energy dispersive spectrometry elemental mappings (figure 1(g)) show that the MnO nanoparticles are homogeneously distributed in the GS/CNT matrix by the uniform dispersed Mn, O, and C elements in the selected area.

### 3.2. Structure and composition analysis

The purity and crystalline phase of the MnO@GS/CNT sample were characterized by XRD analysis. As shown in figure 2(a), the diffraction peaks located at  $35.0^\circ$ ,  $40.6^\circ$ ,  $58.8^\circ$ ,  $70.2^\circ$ , and  $73.8^\circ$  can be attributed to pure face-centered cubic MnO (JCPDS# 07-0230) [20, 25]. Besides, the weak diffraction peak at about  $25^\circ$  is assigned to CNT and the broad hump at around  $23^\circ$  is in accord with the characteristic peak (002) of graphite [34, 39]. Raman spectroscopy was subsequently carried out to confirm the existence of MnO and carbonaceous materials. As depicted in figure 2(b), two prominent peaks at about  $1327$  and  $1575\text{ cm}^{-1}$  are indexed to the

$A_{1g}$  vibration of the defect-induced mode (D band) and the  $E_{2g}$  graphitic mode (G band), respectively [40, 41]. The intensity ratio of D versus G band ( $I_D/I_G$ ) is 1.24, which represents the structural imperfection of  $sp^3$ -type disordered carbon materials [42]. This result indicates the presence of abundant defects and vacancies in the GS/CNT networks, which could not only offer more intercalation sites for lithium storage, but also enhance the ionic conductivity of the electrolyte while maintaining excellent electrical conductivity, contributing to the total capacity. Additionally, the peak at  $645\text{ cm}^{-1}$  is assigned to the vibration of Mn–O bonds, further confirming the presence of MnO in MnO@GS/CNT [23, 33]. The carbon content of MnO@N-GSC/GR was evaluated by TGA, as shown in figure 2(c). Based on the 7.5 wt.% increase of weight from MnO to  $\text{Mn}_3\text{O}_4$  [39], the weight fraction of carbon in MnO@GS/CNT is about 34.1%. It should be noted that the negligible weight decrease of MnO@GS/CNT below  $200^\circ\text{C}$  could be attributed to the evaporation of adsorbed water. The surface element composition and valence of MnO@GS/CNT were determined by XPS. In the XPS survey

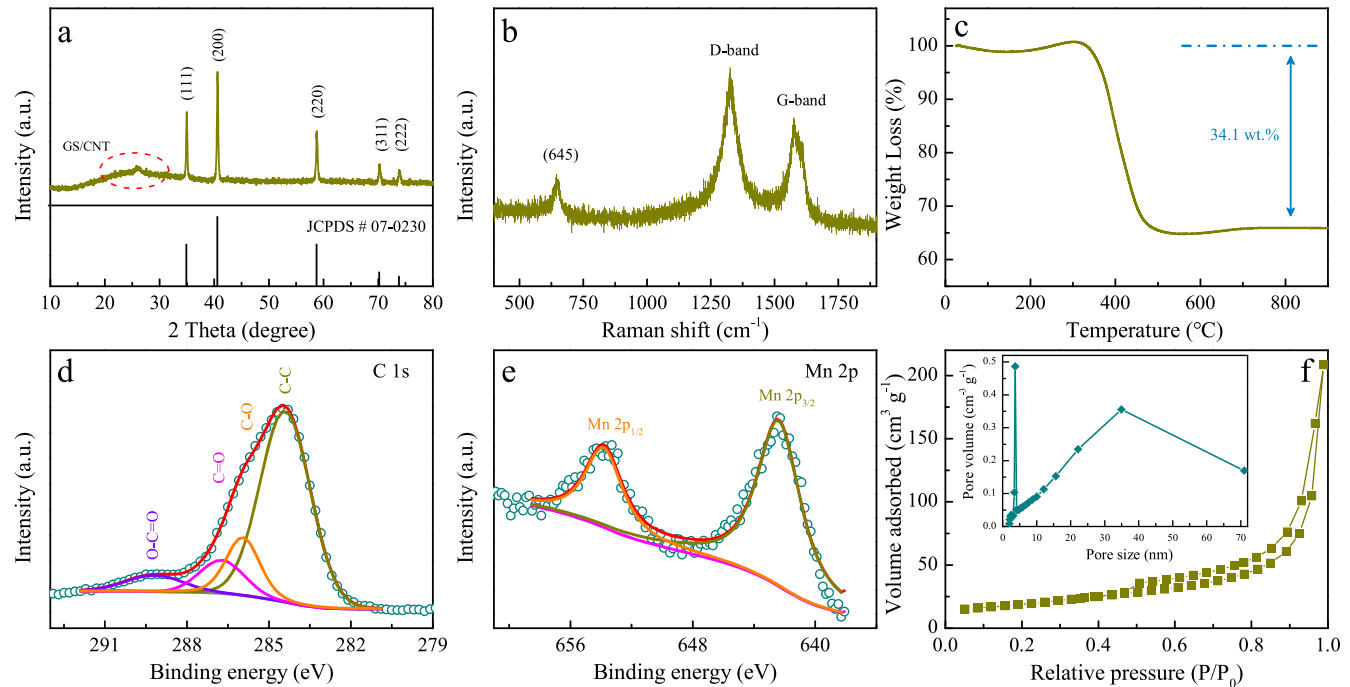


**Figure 2.** (a) XRD patterns; (b) Raman spectra; (c) TGA curve; (d) high-resolution XPS spectra of C 1s; (e) high-resolution XPS spectra of Mn 2p and (f)  $N_2$  adsorption–desorption isotherms (the inset presents the corresponding pore size distribution curve) of MnO@GS/CNT composite.

spectra (figure S3), the characteristic peaks of Mn, C, and O can be clearly observed, with no evidence of impurities. Four fitted peaks in the XPS C 1s spectrum (figure 2(d)) are ascribed to graphitic carbon (284.5 eV), C–O (285.9 eV), C=O (286.7 eV), and O=C–O (289.3 eV), respectively [29]. A prime O 1s peak at 533.5 eV appears (figure S4), further indicating the presence of remained  $O^{2-}$  species linked by C atoms in GS or CNT [36]. The high-resolution spectrum of Mn 2p (figure 2(e)) exhibits two peaks at 642.5 eV for Mn 2p<sub>3/2</sub> and 653.9 eV for Mn 2p<sub>1/2</sub>, respectively, a typical characteristic of MnO phase [26]. Nitrogen adsorption–desorption measurements were performed and the results are shown in figure 2(f) and S5. It could be seen that the isotherm rises rapidly with the increase of  $P/P_0$  due to the capillary condensation and the isotherm of desorption and absorption is not overlapped, leading to the adsorption hysteresis. The existed hysteresis loops between adsorption and desorption isotherm curves, representing the mesoporous characteristics. And the pore size distribution curves indicate that MnO@GS/CNT has abundant macro- and meso- porous than MnO. Moreover, the BET surface area of MnO@GS/CNT and MnO are calculated to be 67.7 and  $3.74\text{ m}^2\text{ g}^{-1}$ , respectively. Such porous architecture with high surface area of MnO@GS/CNT is favorable for efficient electrolyte penetrate into the inner electrode material and rapid lithium ions diffusion. Moreover, it is also able to accommodate the volumetric change of MnO during the conversion process, ensuring a relatively high capacity and excellent cycling stability.

### 3.3. Energy storage applications

The electrochemical performance of MnO@GS/CNT as anode material for LIBs was first investigated by cyclic voltammograms (CV). The CV curves of the initial five cycles for MnO@GS/CNT (figure 3(a)) were collected at a scan rate of  $0.5\text{ mV s}^{-1}$  in the potential range of 0.02–3.0 V versus Li/Li<sup>+</sup> using Li metal as the counter and reference electrode. In the initial cathodic scan, two reduction peaks at around 0.61 and 0.15 V can be observed, corresponding to the irreversible reaction associated with the electrolyte decomposition and formation of SEI films and the evolution from Mn<sup>2+</sup> to Mn<sup>0</sup> by reduction reaction ( $\text{MnO} + 2\text{Li}^+ + 2\text{e}^- \rightarrow \text{Mn} + \text{Li}_2\text{O}$ ), respectively [24, 26]. In the initial anodic scan, the oxidation peak at around 1.3 V is attributed to the reversible oxidation of Mn to Mn<sup>2+</sup> ( $\text{Mn} + \text{Li}_2\text{O} \rightarrow \text{MnO} + 2\text{Li}^+ + 2\text{e}^-$ ). One additional oxidation peak appears at around 2.1 V corresponds to the further oxidation of Mn<sup>2+</sup> to higher oxidation state, which is not observed for bare MnO electrode (figure S6) [32]. This phenomenon could be attributed to the boosted charge/transfer kinetics and the reaction activity in the MnO@GS/CNT anode, which can contribute extra reversible capacity in the following cycles [35, 37]. It is worth noting that the cathodic peak shifts to 0.33 V, further demonstrating the improved kinetics and evolutions in the microstructure of the hybrid electrode in the following cycles [25, 36, 38].

Figure 3(b) presents typical galvanostatic discharge–charge profiles for the initial five cycles of MnO@GS/CNT at a current density of  $0.2\text{ A g}^{-1}$ . In consistence with the CV

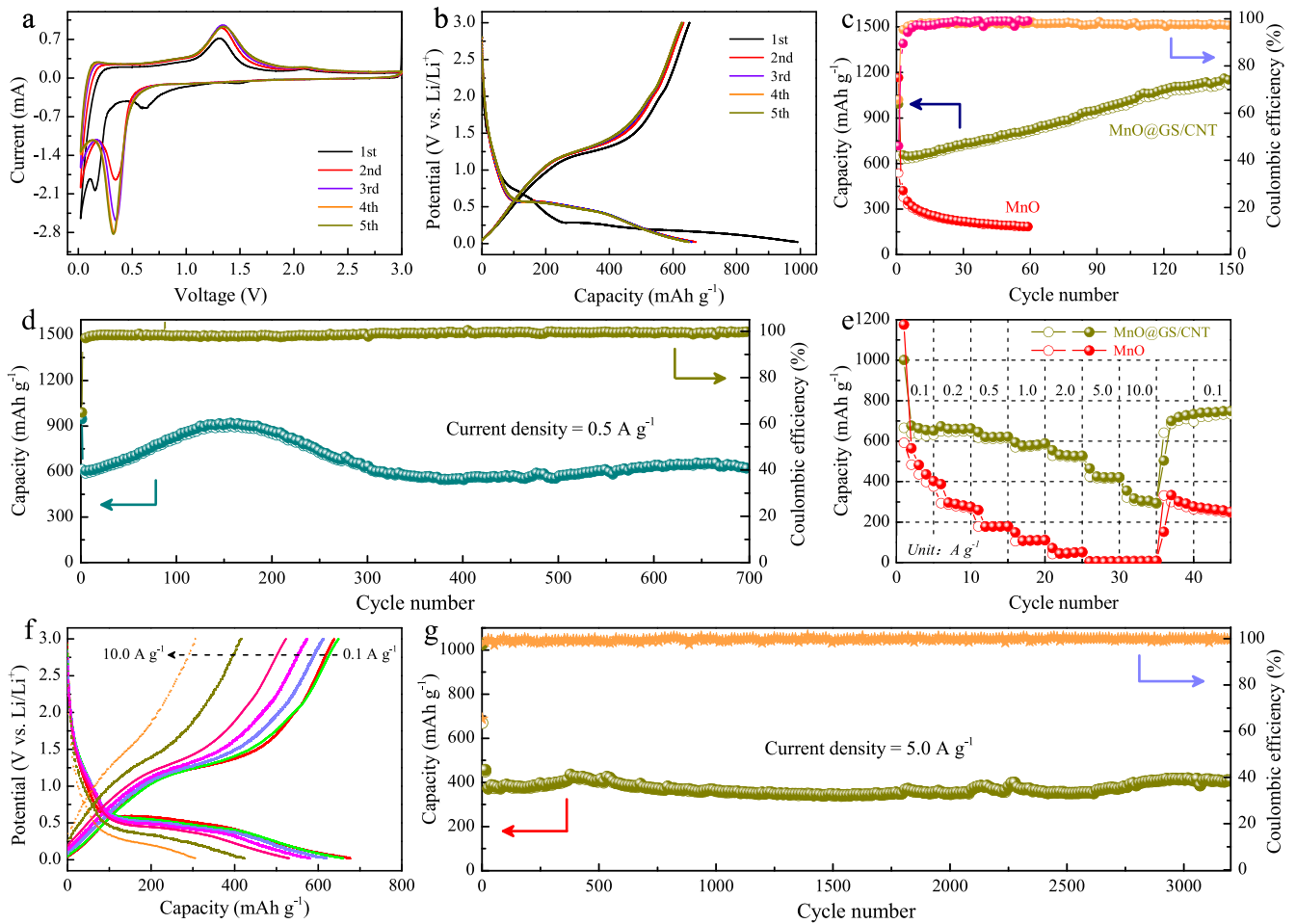


**Figure 3.** (a) CV curves for the initial five cycles of MnO@GS/CNT anode at a scan rate of  $0.5 \text{ mV s}^{-1}$ ; (b) galvanostatic charge–discharge profiles for the initial five cycles of MnO@GS/CNT anode at a current density of  $0.2 \text{ A g}^{-1}$ ; (c) cycling performance at a current density of  $0.2 \text{ A g}^{-1}$  of MnO@GS/CNT anode, with bare MnO for comparison; (d) cycling performance at a current density of  $0.5 \text{ A g}^{-1}$  of MnO@GS/CNT anode; (e) rate performance at different current densities from  $0.1$  to  $10 \text{ A g}^{-1}$  of MnO@GS/CNT anode, with bare MnO for comparison; (f) galvanostatic charge–discharge profiles of MnO@GS/CNT anode at different current densities; (g) cycling performance at a current density of  $5 \text{ A g}^{-1}$  and corresponding Coulombic efficiency (CE) of MnO@GS/CNT anode.

results, a distinct discharge voltage plateau at about  $0.3 \text{ V}$  as well as the corresponding sloped charge plateaus between  $1.2$  and  $1.5 \text{ V}$  can be clearly observed in the first discharge–charge profiles. The MnO@GS/CNT anode delivers a high initial discharge capacity of  $991 \text{ mAh g}^{-1}$  and a charge capacity of  $651 \text{ mAh g}^{-1}$  at  $0.2 \text{ A g}^{-1}$ , corresponding to an initial CE of  $65.8\%$ . The initial irreversible capacity loss is attributed to the consumption of lithium ions during the formation of SEI film and the irreversible insertion of lithium ions into the defects on the GS and CNT [21, 24]. This problem could be solved through prelithiation technique or the incorporation of sacrificial Li salt additives [43, 44]. Afterward, the CE significantly increases to  $94.2\%$ ,  $95.4\%$ , and  $96.4\%$  for the second, third, and fourth cycle, suggesting the rapid stabilization of the SEI film. Interestingly, after 60 cycles, the discharge capacity of the MnO@GS/CNT anode slightly increases to  $823 \text{ mAh g}^{-1}$ . In contrast, although MnO delivers a higher initial discharge capacity of  $1166 \text{ mAh g}^{-1}$ , only around  $184 \text{ mAh g}^{-1}$  is maintained after 60 cycles (figure 3(c)). Remarkably, a reversible capacity as high as  $1143 \text{ mAh g}^{-1}$  is achieved for MnO@GS/CNT after 150

cycles at  $0.2 \text{ A g}^{-1}$ , much higher than the theoretical value of manganese oxides. Such an activation process could be derived from the gradually activation of the electrode materials for the gradual permeation of the electrolyte into the porous GS/CNT [39], and the generation of higher oxidation state manganese, as demonstrated in the charge–discharge voltage profiles of MnO@GS/CNT at different cycles (figure S7). Notably, the corresponding slope at around  $2.1 \text{ V}$  in the charge process becomes more gently, introducing more extra capacity. Moreover, cycling performance of MnO@GS/CNT was also operated at the current density of  $0.5 \text{ A g}^{-1}$ , as demonstrated in figure 3(d). Similar to the cycling test at  $0.2 \text{ A g}^{-1}$  (figure 3(c)), the discharge capacity also increases gradually to as high as  $921 \text{ mAh g}^{-1}$  as well from the beginning to the 158 cycles when cycled at  $0.5 \text{ A g}^{-1}$ . This phenomenon of ever-increasing capacity can be also attributed to the gradual permeation of lithium ions [39], and the generation of higher oxidation state manganese [35]. After that, the capacity eases back and remains stable for the subsequent cycles. With prolonged cycling over 700 cycles, the MnO@GS/CNT anode can still deliver a high reversible

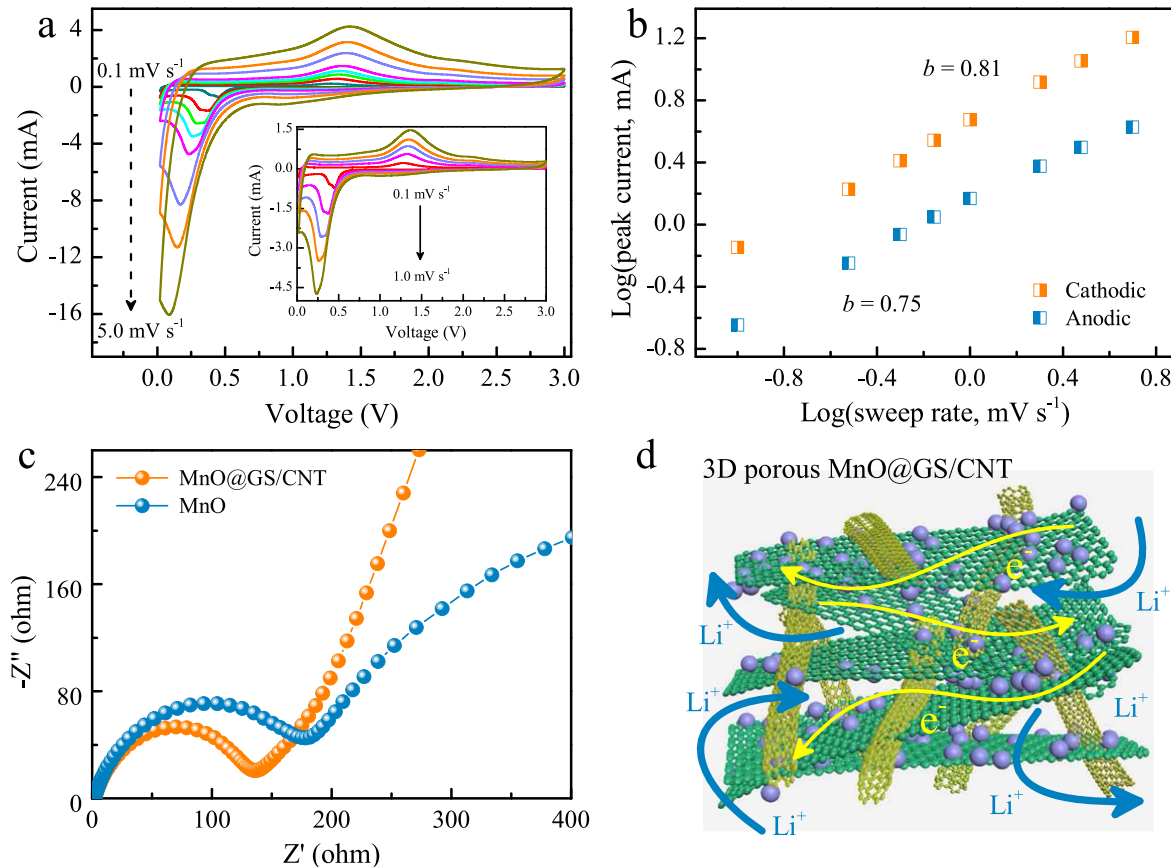


**Figure 4.** (a) CV curves of MnO@GS/CNT anode at various sweep rates from  $0.1$  to  $5\text{ mV s}^{-1}$ ; (b) determination of the  $b$  value using the relationship between peak current and scan rate; (c) electrochemical impedance spectroscopy of bare MnO and MnO@GS/CNT anode; (d) summary of the enhanced electrochemical performance mechanism of the 3D porous MnO@GS/CNT architecture in lithium-ion batteries.

capacity of  $616\text{ mAh g}^{-1}$ , indicating the superb cycling stability.

The rate performance of MnO@GS/CNT anode at various current densities from  $0.1$  to  $10.0\text{ A g}^{-1}$  is displayed in figure 3(e). The MnO@GS/CNT anode could deliver the average reversible capacity of  $677$ ,  $600$ ,  $620$ ,  $580$ , and  $530\text{ mAh g}^{-1}$  at  $0.1$ ,  $0.2$ ,  $0.5$ ,  $1.0$ , and  $2.0\text{ A g}^{-1}$ , respectively, much higher than those of bare MnO. Even at high current density of  $5.0$  and  $10.0\text{ A g}^{-1}$ , the average reversible capacity still reach as high as  $422$  and  $306\text{ mAh g}^{-1}$ , respectively, which are demonstrated in the charge and discharge curves in figure 3(f). It is worth pointing out that when the current density is reversed to  $0.1\text{ A g}^{-1}$ , the reversible capacity could swiftly return and gradually increase to  $750\text{ mAh g}^{-1}$ , highlighting the strong tolerance for fast lithiation/delithiation and good cycling stability of the MnO@GS/CNT anode. In contrast, the bare MnO exhibits relatively inferior rate performance, which can only maintain a negligible capacity of  $5\text{ mAh g}^{-1}$  at  $5.0\text{ A g}^{-1}$ . In order to better evaluate the capacity difference between the two anode materials, the rate and cycling tests of the corresponding carbon content GS/CNT were investigated and shown in figure S8. The GS/CNT electrodes reveal a good rate performance and cycle stability due to its high specific surface area and excellent conductivity. Therefore, the significantly enhanced rate capability and cycle stability of MnO@GS/CNT can be

attributed to the improved electrical conductivity and surface pseudocapacitance originating from the synergistic effect of GS/CNT and MnO nanoparticles. The 3D porous MnO@GS/CNT architecture with interconnected networks of 1D CNT and 2D GS not only offers shorter ion diffusion lengths and fast ion/electron transport channels, but also provides large active surface area and internal voids to accommodate electrolyte penetration for efficient ion access and volume changes of MnO. Besides, a bare MnO@GS/CNT electrode without the addition of carbon black was also tested to evaluate the natural electrochemical properties of MnO@GS/CNT. As shown in figure S9, the bare MnO@GS/CNT electrode exhibits considerable rate capability and cycle stability, further demonstrating the intrinsic fast and efficient electronic/ionic conductivity of MnO@GS/CNT. Furthermore, the MnO@GS/CNT anode exhibits an impressive cycle lifespan at a high current density of  $5.0\text{ A g}^{-1}$  (figure 3(g)). After the activation process in the initial 18 cycles, a high reversible capacity of  $406\text{ mAh g}^{-1}$  over 3200 cycles is still achieved, more than the theoretical capacity of graphite ( $\sim 372\text{ mAh g}^{-1}$ ), further evidence for its superior electrochemical performance. Compared with previously reported other TMOs/carbon hybrid anode materials, the MnO@GS/CNT anode exhibits excellent long-term cycling stability even under the fast and deep discharge–charge processes, as summarized in table S1.

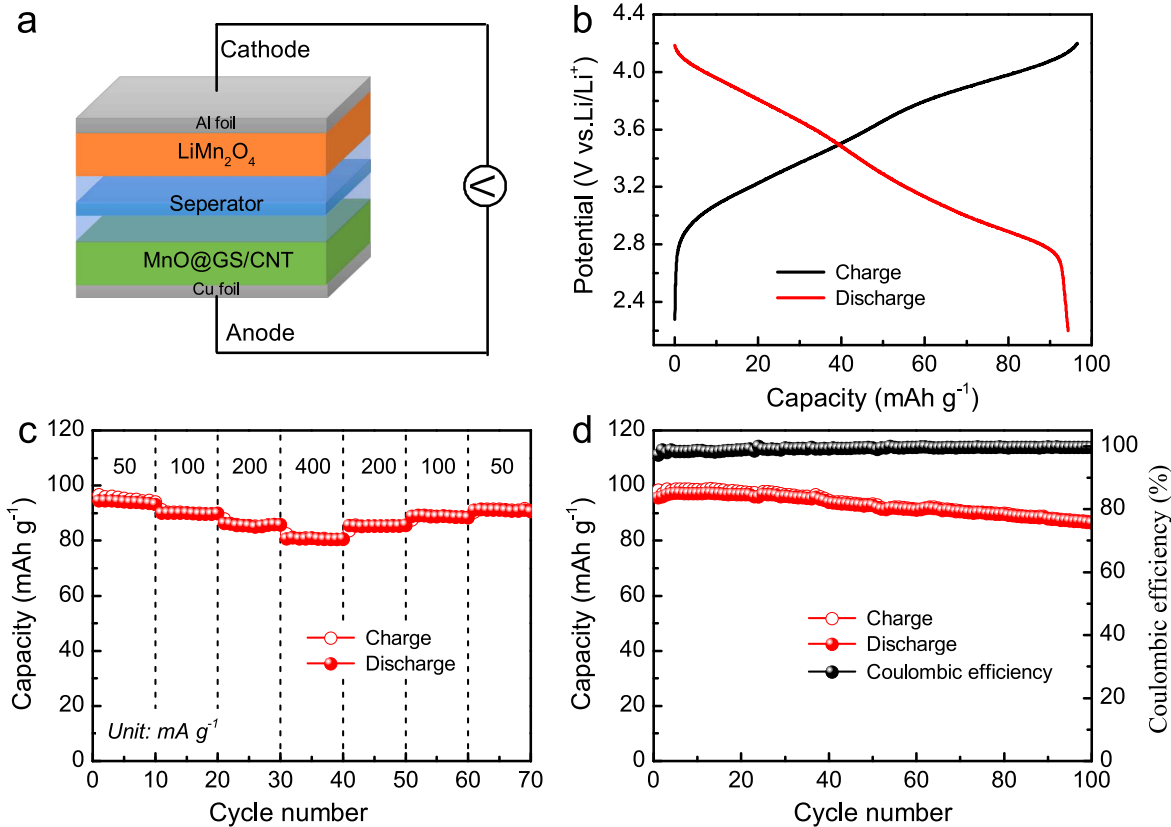


**Figure 5.** (a) Schematic presentation of the LMO||MnO@GS/CNT full cell; (b) galvanostatic charge–discharge profile of the LMO||MnO@GS/CNT full cell; (c) rate performance at different current densities of LMO||MnO@GS/CNT full cell; (d) cycling performance at a current density of 100 mA g<sup>−1</sup> and corresponding Coulombic efficiency of LMO||MnO@GS/CNT full cell.

Assuming conventional diffusion-controlled electrochemical behaviors of MnO-based anode material, it is practically impossible to achieve remarkable rate capability and excellent cycling performance. Considering the specially designed 3D MnO@GS/CNT with large surface area, void spaces, and interstitial sites, pseudocapacitance storage, characterized by surface-controlled behavior, might account for the superior electrochemical performance of the MnO@GS/CNT anode. To elucidate the electrochemical kinetics of this nanocomposite electrode, a kinetic analysis was conducted for a half-cell. Figure 4(a) presents the representative CV curves of the MnO@GS/CNT anode at various sweep rates ranging from 0.1 to 5.0 mV s<sup>−1</sup>. The redox peaks with no significant shape change could be clearly observed in the corresponding CV curves with increasing sweep rate from 0.1 to 1.0 mV s<sup>−1</sup>. Moreover, the shape is well preserved and the peak voltage shifts with sweep rate are quite small in comparison to that of bare MnO (figure S10), suggesting small polarization and fast reaction kinetics of MnO@GS/CNT. Generally, the current (*i*) and sweep rates (*v*) obey the following power law:  $i = av^b$ , where *a* and *b* are adjustable values [45]. The *b* value reflects the types of the charge storage mechanism, which can be determined by the slope of the log(*v*)–log(*i*) plots as shown in figure 4(b). Specifically, the *b* value of 0.5 represents an ideally diffusion-controlled process, whereas 1.0 represents an ideally surface-controlled process. The calculated *b* values of cathodic and

anodic peaks are 0.81 and 0.75, respectively, which can be quantified at sweep rates ranging from 0.01 to 5.0 mV s<sup>−1</sup>. It demonstrates that the lithium storage of MnO@GS/CNT presents pseudocapacitive characteristics, conducing to fast charge storage and long-term cyclability.

In order to further understand the effect of GS/CNT conductive network in the MnO@GS/CNT anode, EIS was performed and the results are shown in figure 4(c). All the Nyquist plots of MnO and MnO@GS/CNT consist of a semicircle in the medium frequency region followed by a sloped curve in the low frequency region, corresponding to the charge transfer resistance between electrolyte and electrode as well as the solid-state diffusion of lithium ions in active materials. Obviously, MnO@GS/CNT exhibits a lower charge transfer resistance than MnO, confirming the increased charge transfer process in the presence of the conductive additives. Besides, the more sloped curve in the low frequency region demonstrates the effectively rapid diffusion of lithium ions, which is essential for fast and reversible lithium storage. According to the above analyses, the impressive electrochemical performance of MnO@GS/CNT composite with 3D porous interconnected architecture could be attributed to the following reasons (figure 4(d)). First, the nanoparticles in porous structure shorten the ion diffusion pathway in MnO, facilitating the conversion reaction kinetics. Second, the interpenetrated 3D architecture with high specific surface areas could not only enhance the interface of electrode/

electrolyte, but also provide multidimensional pathways for efficient electron transport for the electrochemical reaction of MnO. Third, the porous structure of MnO@GS/CNT with abundant well-developed bimodal-mesoporous can synergistically alleviate of the volume expansion of MnO and guarantee the integrated mass-transportation network during cycling process, ensuring long-cycle life at high current density.

Above merits suggest that the as-prepared MnO@GS/CNT has highly appealing electrochemical properties as an anode for a complete Li-ion battery cell. To demonstrate a manganese-oxide based LIB, the MnO@GS/CNT anode and LiMn<sub>2</sub>O<sub>4</sub> cathode were assembled into a full cell, as schematically illustrated in figure 5(a). Figure 5(b) shows the galvanostatic discharge-charge profile of LMO || MnO@GS/CNT cycled between 2.2 and 4.2 V at 50 mA g<sup>-1</sup>. The profile of full cell exhibits steep slopes compared to that of LiMn<sub>2</sub>O<sub>4</sub> half-cell (figure S11), which is mainly attributed to the inherent voltage characteristics of MnO@GS/CNT. More importantly, the LMO || MnO@GS/CNT battery can output an average voltage of 3.4 V and deliver charge/discharge capacities of 96.6/94.4 mAh g<sup>-1</sup> based on the cathode mass. The rate performance of the full cell is presented in figure 5(c). The capacity retentions at 400 mA g<sup>-1</sup> is about 85% relative to the capacity at 50 mA g<sup>-1</sup>, which is close to the value of LiMn<sub>2</sub>O<sub>4</sub> half-cell (figure S12), showing excellent rate capability. When the rate is recovered, the capacity is completely restored, indicating the remarkable electrochemical reversibility of the full cell. More significantly, the cycling stability was further evaluated, as shown in figure 5(d). Although the capacity slowly fade from the beginning, it still retains 90% after 100 cycles, indicating an outstanding cycling stability of the full cell. All of these demonstrate the potential of MnO@GS/CNT anode practical application in advanced LIB.

#### 4. Conclusion

In summary, an efficient and facile approach to developing the well-distributed MnO nanoparticles in 3D cross-linked graphene/CNT networks has been demonstrated to achieve pronounced electrochemical performance. Benefiting from the synergistic interaction of highly conductive matrix and 3D bimodal-mesoporous architecture, the as-built MnO@GS/CNT structure effectively accommodate the volume changes of MnO and facilitate electron/ion transfer, boosting the electrochemical activity toward lithium storage. The nanocomposite anode exhibits an ultrahigh reversible capacity (1143 mAh g<sup>-1</sup> at 0.2 A g<sup>-1</sup>), excellent rate capability (306 mAh g<sup>-1</sup> at ultrahigh rate of 10.0 A g<sup>-1</sup>), as well as long-term stable cyclability at high rate (405 mAh g<sup>-1</sup> over 3200 cycles at 5.0 A g<sup>-1</sup>). When assembled the MnO@GS/CNT anode and LiMn<sub>2</sub>O<sub>4</sub> cathode into a full cell, it also can deliver remarkable rate capability and cycling stability. All these data indicate the promising application of 3D porous MnO@GS/CNT for high property anode in LIB. It is expected that this simple and scalable method will extend to other conversion-type anode materials for enhancing the lithium storage performance.

#### Acknowledgments

This work was financially supported by the National Key Research and Development Program of China (Grant No. 2017YFA0303403), the Natural Science Foundation of China (Grant Nos. 61674057, 61504156, and 61227902), the Projects of Science and Technology Commission of Shanghai Municipality (Grant Nos. 18JC1412400 and 15JC1401600), and the Program for Professor of Special Appointment (Eastern Scholar) at Shanghai Institutions of Higher Learning and the Fundamental Research Funds for the Central Universities.

#### ORCID iDs

Zhigao Hu  <https://orcid.org/0000-0003-0575-2191>

#### References

- [1] Armand M and Tarascon J M 2008 Building better batteries *Nature* **451** 652–7
- [2] Goodenough J B 2014 Electrochemical energy storage in a sustainable modern society *Energy Environ. Sci.* **7** 14–9
- [3] Tang Y X, Zhang Y Y, Li W L, Ma B and Chen X D 2015 Rational material design for ultrafast rechargeable lithium-ion batteries *Chem. Soc. Rev.* **44** 5926–40
- [4] Sun H T *et al* 2017 Three-dimensional holey-graphene/nioobia composite architectures for ultrahigh-rate energy storage *Science* **356** 599–604
- [5] Lyu Z Y, Yang L J, Xu D, Zhao J, Lai H W, Jiang Y F, Wu Q, Li Y, Wang X Z and Hu Z 2015 Hierarchical carbon nanocages as high-rate anodes for Li- and Na-ion batteries *Nano Res.* **8** 3535–43
- [6] Jiang J, Li Y, Liu J, Huang X, Yuan C and Lou X W 2012 Recent advances in metal oxide-based electrode architecture design for electrochemical energy storage *Adv. Mater.* **24** 5166–80
- [7] Reddy M V, Rao G V S and Chowdari B V R 2013 Metal oxides and oxysalts as anode materials for Li ion batteries *Chem. Rev.* **113** 5364–457
- [8] Srivastava M, Singh J, Kuila T, Layek R K, Kime N H and Lee J H 2015 Recent advances in graphene and its metal-oxide hybrid nanostructures for lithium-ion batteries *Nanoscale* **7** 4820–68
- [9] Zhang K, Han X P, Hu Z, Zhang X L, Tao Z T and Chen J 2015 Nanostructured Mn-based oxides for electrochemical energy storage and conversion *Chem. Soc. Rev.* **44** 699–728
- [10] Bruce P G, Scrosati B and Tarascon J M 2008 Nanomaterials for rechargeable lithium batteries *Angew. Chem., Int. Ed. Engl.* **17** 2930–46
- [11] Choi S H, Lee J K and Kang Y C 2015 Three-dimensional porous graphene-metal oxide composite microspheres: preparation and application in Li-ion batteries *Nano Res.* **8** 1584–94
- [12] Wang Z Y, Zhou L and Lou X W 2012 Metal oxide hollow nanostructures for lithium-ion batteries *Adv. Mater.* **24** 1903–11
- [13] Hu J K, Sun C F, Gillette E, Gui Z, Wang Y H and Lee S B 2016 Dual-template ordered mesoporous carbon/Fe<sub>2</sub>O<sub>3</sub> nanowires as lithium-ion battery anodes *Nanoscale* **18** 12958–69
- [14] Xia L, Wang S Q, Liu G X, Ding L X, Li D D, Wang H H and Qiao S Z 2016 Flexible SnO<sub>2</sub>/N-doped carbon nanofiber films as integrated electrodes for lithium-ion batteries with superior rate capacity and long cycle life *Small* **12** 853–9

- [15] Tang J, Liu W, Wang H L and Gomez A 2016 High performance metal oxide-graphene hybrid nanomaterials synthesized via opposite-polarity electrosprays *Adv. Mater.* **28** 10298–303
- [16] Liu L, Yang X F, Lv C X, Zhu A M, Zhu X Y, Guo S J, Chen C M and Yang D J 2016 Seaweed-derived route to Fe<sub>2</sub>O<sub>3</sub> hollow nanoparticles/N-doped graphene aerogels with high lithium ion storage performance *ACS Appl. Mater. Interfaces* **8** 7047–53
- [17] Zhong K F, Xia X, Zhang B, Li H, Wang Z X and Chen L Q 2010 MnO powder as anode active materials for lithium ion batteries *J. Power Sources* **195** 3300–8
- [18] Zhang K et al 2012 Synthesis of nitrogen-doped MnO/graphene nanosheets hybrid material for lithium ion batteries *ACS Appl. Mater. Interfaces* **4** 658–64
- [19] Xu G L, Xu Y F, Sun H, Fu F, Zheng X M, Huang L, Li J T, Yang S H and Sun S G 2012 Facile synthesis of porous MnO/C nanotubes as a high capacity anode material for lithium ion batteries *Chem. Commun.* **48** 8502–4
- [20] Sun Y M, Hu X L, Luo W, Xia F F and Huang Y H 2013 Reconstruction of conformal nanoscale MnO on graphene as a high-capacity and long-life anode material for lithium ion batteries *Adv. Funct. Mater.* **23** 2436–44
- [21] Xia Y et al 2013 Green and facile fabrication of hollow porous MnO/C microspheres from microalgae for lithium-ion batteries *ACS Nano* **7** 7083–92
- [22] Guo J C, Liu Q, Wang C S and Zachariah M R 2012 Interdispersed amorphous MnO<sub>x</sub>-carbon nanocomposites with superior electrochemical performance as lithium-storage material *Adv. Funct. Mater.* **22** 803–11
- [23] Zhang W, Sheng J Z, Zhang J, He T, Hu L, Wang R, Mai L Q and Mu S C 2016 Hierarchical three-dimensional MnO nanorods/carbon anodes for ultralong-life lithium-ion batteries *J. Mater. Chem. A* **4** 16936–45
- [24] Jiang H, Hu Y J, Guo S J, Yan C Y, Lee P S and Li C Z 2014 Rational design of MnO/carbon nanopeapods with internal void space for high-rate and long-life Li-ion batteries *ACS Nano* **8** 6038–46
- [25] Wang J G, Zhang C B, Jin D D, Xie K Y and Wei B Q 2015 Synthesis of ultralong MnO/C coaxial nanowires as freestanding anodes for high-performance lithium ion batteries *J. Mater. Chem. A* **3** 13699–705
- [26] Sun Q, Wang Z J, Zhang Z J, Yu Q, Qu Y, Zhang J Y, Yu Y and Xiang B 2016 Rational design of graphene-reinforced MnO nanowires with enhanced electrochemical performance for Li-ion batteries *ACS Appl. Mater. Interfaces* **8** 6303–8
- [27] Wang S B, Xiao C L, Xing Y L, Xu H Z and Zhang S C 2015 Formation of a stable carbon framework in a MnO yolk-shell sphere to achieve exceptional performance for a Li-ion battery anode *J. Mater. Chem. A* **3** 15591–997
- [28] Zhang L L, Ge D H, Qu G L, Zheng J W, Cao X Q and Gu H W 2017 Formation of porous nitrogen-doped carbon-coating MnO nanospheres for advanced reversible lithium storage *Nanoscale* **9** 5451–7
- [29] Gu X, Yue J, Chen L, Liu S, Xu H Y, Yang J, Qian Y T and Zhao X B 2015 Coaxial MnO/N-doped carbon nanorods for advanced lithium-ion battery anodes *J. Mater. Chem. A* **3** 1037–41
- [30] Zhang W, Sheng J, Zhang J, He T, Hu L, Wang R, Mai L Q and Mu S C 2016 Hierarchical three-dimensional MnO nanorods/carbon anodes for ultralong-life lithium-ion batteries *J. Mater. Chem. A* **4** 16936–45
- [31] Wang S B, Xing Y L, Xiao C L, Xu H Z and Zhang S C 2016 A peapod-inspired MnO@C core–shell design for lithium ion batteries *J. Power Sources* **307** 11–6
- [32] Liu D H, Lu H Y, Wu X L, Hou B H, Wan F, Bao S D, Yan Q Y, Xie H M and Wang R S 2015 Constructing the optimal conductive network in MnO-based nanohybrids as high-rate and long-life anode materials for lithium-ion batteries *J. Mater. Chem. A* **3** 19738–46
- [33] Xiao Y and Cao M H 2015 Carbon-anchored MnO nanosheets as an anode for high-rate and long-life lithium-ion batteries *ACS Appl. Mater. Interfaces* **7** 12840–9
- [34] Zhang Q T, Dai Q Q, Li M, Wang X M and Li A 2016 Incorporation of MnO nanoparticles inside porous carbon nanotubes originated from conjugated microporous polymers for lithium storage *J. Mater. Chem. A* **4** 19132–9
- [35] Yuan T Z, Jiang Y Z, Sun W P, Xiang B, Li Y, Yan M, Xu B and Dou S X 2016 Ever-increasing pseudocapacitance in RGO-MnO-RGO sandwich nanostructures for ultrahigh-rate lithium storage *Adv. Funct. Mater.* **26** 2198–206
- [36] Zhang W, Li J N, Zhang J, Sheng J Z, He T, Tian M Y, Zhao Y F, Xie C J, Mai L Q and Mu S C 2017 Top-down strategy to synthesize mesoporous dual carbon armored MnO nanoparticles for lithium-ion battery anodes *ACS Appl. Mater. Interfaces* **9** 12680–6
- [37] Wang S B, Xing Y L, Xu H Z and Zhang S C 2014 MnO nanoparticles interdispersed in 3D porous carbon framework for high performance lithium-ion batteries *ACS Appl. Mater. Interfaces* **6** 12713–8
- [38] Chen L F, Ma S X, Lu S, Feng Y, Zhang J, Xin S and Yu S H 2017 Biota templated synthesis of three-dimensional porous MnO/C-N nanocomposites from renewable rapeseed pollen: an anode material for lithium-ion batteries *Nano Res.* **10** 1–11
- [39] Zhang Y, Chen P H, Gao X, Wang B, Liu H, Wu H, Liu H K and Dou S X 2016 Nitrogen-doped graphene ribbon assembled core-sheath MnO@graphene scrolls as hierarchically ordered 3D porous electrodes for fast and durable lithium storage *Adv. Funct. Mater.* **26** 7754–65
- [40] Kudin K N, Ozbas B, Schniepp H C, Prudhomme R K, Aksay I A and Car R 2008 Raman spectra of graphite oxide and functionalized graphene sheets *Nano Lett.* **8** 36–41
- [41] He J R, Chen Y F, Li P J, Fu F, Wang Z G and Zhang W L 2015 Three-dimensional CNT/graphene-sulfur hybrid sponges with high sulfur loading as superior-capacity cathodes for lithium-sulfur batteries *J. Mater. Chem. A* **3** 18605–10
- [42] Zhang J, Zhang W, He T, Amiuu I S, Kou Z K, Li J N and Mu S C 2017 Smart reconstruction of dual-carbon decorated MnO for anode with high-capacity and ultralong-life lithium storage properties *Carbon* **115** 95–104
- [43] Hassoun J, Lee K S, Sun Y K and Scrosati B 2011 An advanced lithium ion battery based on high performance electrode materials *J. Am. Chem. Soc.* **133** 3139–43
- [44] Sun Y, Lee H W, Seh Z W, Liu N, Sun J, Li Y and Cui Y 2016 High-capacity battery cathode prelithiation to offset initial lithium loss *Nat. Energy* **1** 15008
- [45] Lindström H, Södergren S, Solbrand A, Rensmo H, Hjelm J, Hagfeldt A and Lindquist S E 1997 Li<sup>+</sup> ion insertion in TiO<sub>2</sub> (Anatase). 2. Voltammetry on nanoporous films *J. Phys. Chem. B* **101** 7717–22